Efficient Mode Converter and Orbital-Angular-Momentum Generator via Gradient-Index Metamaterials

Chuanjie Hu and Huanyang Chen*

Institute of Electromagnetics and Acoustics and Key Laboratory of Electromagnetic Wave Science and Detection Technology, Xiamen University, Xiamen 361005, China

(Received 18 August 2020; revised 15 October 2020; accepted 23 December 2020; published 20 January 2021)

As the predominant information carrier, acoustic waves play an essential role in underwater communications, with significantly less scattering and attenuation than that of electromagnetic waves. Integrating the gradient-index metamaterials (GIMs) with circular waveguide, we propose a design to achieve a multimodal acoustic converter with multifrequency and great efficiency in a circular waveguide. Numerical simulations and analytical results demonstrate that the zeroth order of acoustic mode can be converted to the first-order mode or even higher-order modes. Moreover, optimizing the parameter of GIMs, it is further demonstrated that GIMs, attached to the rigid wall of waveguide, can be utilized as a passive orbital-angular-momentum (OAM) generator. In the future, this mode-conversion scheme with suppressed backscattering and high mode-conversion efficiency may find many applications in integrated acoustics and underwater communications.

DOI: 10.1103/PhysRevApplied.15.014035

I. INTRODUCTION

Oceans are a significant part of the earth system, which human beings depend on. Recently, underwater acoustic communications have received much attention as the attenuation of acoustics is at least 3 orders of intensity smaller than that of electromagnetic waves [1,2]. The significant loss of microwave and powerful scattering of visible light essentially result in a great suppression of light waves. However, compared with electromagnetic waves, acoustic waves (as a scalar wave) do not have the degree of freedom for polarizations or spin. Moreover, the capacity of communication channels with acoustic waves is also restricted by the low operating frequency (under 20 kHz) and the low inherent speed. How to further expand the bandwidth of acoustic communication has thereby become a key problem to be solved. Recently, mode-division multiplexing (MDM) is a very promising research field in waveguide communication system [3–5]. The capacity of a communication system can be greatly expanded if MDM is used in the mode multiplexer and mode demultiplexer. Mode excitation and mode conversion are two key problems that must be faced in the initial stage of the research of MDM. The mode-order converter, as the basis and premise for the system of MDM to be operated, also finds varieties of applications, including multimode waveguide bends [6], mode-selective switches [7,8], and so on. Besides, acoustic vortex waves with helical phase distribution have been extended to open up alternative multiplexing and demultiplexing approaches for high-capacity acoustic communications. As an alternative independent freedom of traditional technology, orbital angular momentum (OAM) is expected to bring a great revolution in underwater acoustic communication. Traditional methods of generating acoustic OAM require active arrays consisting of large numbers of independent transducers or passive material with uneven thickness and helical structure, which limit their practical application potential. Recently, acoustic resonators [9] were used to convert plane waves into an outgoing vortex beam with OAM. However, due to the characteristics of the Helmholtz resonator, the operating frequency is strictly a single frequency and the complex structure of the resonator may not be suitable for device miniaturization. Although the potential of acoustic OAM has been preliminarily demonstrated in the current research, it is far from meeting the requirements of practical application. Therefore, the research on acoustic OAM is in the ascendant process, which is a vigorous scientific research field.

On the other hand, metamaterials have found broad applicability in free-space acoustics, including sound attenuation [10], negative refraction [11,12], acoustic imaging [13–15], and many other acoustic devices based on transformation acoustics [16,17]. With the rapid development, soft porous silicone rubber materials have been implemented to a broad range of tunable acoustic refractive index n (from 1.5 to 25 with respect to water) depending on the material porosity ϕ [18,19]. It is worth mentioning that there is a sudden drop of the longitudinal phase velocity c_L with the increase of porosity ϕ, while

*kenyon@xmu.edu.cn

the transverse phase velocity c_T remains constant [18]. The strong dependence of c_L on ϕ has been attributed to the very low value of the shear modulus G_0 (approximately 1 MPa) of the soft elastomeric skeleton (with $\rho \sim 1000$ kg/m^3) [20]. In the fabrication of soft porous silicone materials, the accuracy of target porosity can nearly reach 1% [21], which can be achieved very simply in common polymer-science engineering. It was shown that gradient-index metamaterials can be used to achieve the complete conversion from propagating waves (PWs) to surface waves (SWs) [22]. Recently, its potential to tailor guided waves has drawn a great deal of attention. In particular, by integrating the concept of gradient-index metamaterials into a paralleled-plated waveguide, asymmetric propagation of light without polarization limitations was achieved [23]. This feature leads to plenty of alternative devices, such as mode conversion in a parallel-plate electromagnetic waveguide [24], waveguide cloaking [25,26]. In fact, acoustic waves and water waves are the counterpart of electromagnetic waves, acoustic asymmetric transmission [27], broadband acoustic waveguide cloak [28], and broadband cloak for water waves [29] have also been demonstrated. Therefore, it is desirable that multifunctional mode conversion in an acoustic waveguide can be manipulated in a similar and simple law.

There have been several conventional schemes to achieve mode conversion. For example, it has been suggested that based on the symmetrical match and mismatch between the waveguide mode and the cavity mode, two perpendicular sonic crystal waveguides are connected to achieve even and odd mode conversion [30]. However, those mode-order converters generally have significant backscattering or can only work at a single frequency. According to the coupled-mode theory [31,32], only when the mode converter meets the phase-matching conditions and the field-overlapping conditions, can the high conversion efficiency and the maximum propagation distance be realized. In this paper, we propose a scheme to achieve multimode conversion via integrating asymmetric gradient-index metamaterials (GIMs) into the circular waveguide at multifrequencies. Moreover, we also design an OAM generator based on this mode-conversion theory, which would be very useful in manipulating small particles with acoustic waves [33–35].

II. MODE CONVERTER VIA GRADIENT-INDEX METAMATERIALS

Here our configurations are shown in the schematic diagram in Fig. 1. The proposed structure is a three-dimensional (3D) circular waveguide with the GIMs attached to its outer perfect rigid boundary (PRB) wall. The GIM layer is divided into two symmetrical semiannulus regions. The inner medium is water of radius a, which is coated by a cylindrical layer of GIMs [denoted by the regions in Fig. 1(b) with gradual blue color]. It is obtained by rotating the cross section of the two-dimensional (2D) parallel-plate waveguide in Fig. 1(b) around the propagating direction (z axis).

The index profiles of two semiannulus regions along z direction are

$$n(z) = \begin{cases} 1 + g_i \dfrac{\xi[z + (L/2)]}{2k_0 d}, -\dfrac{L}{2} \le z \le 0, \ i = 1,2 \\ 1 - g_i \dfrac{\xi[z - (L/2)]}{2k_0 d}, 0 \le z \le \dfrac{L}{2}, \quad i = 1,2 \end{cases}, \tag{1}$$

where k_0 is the wave vector in free space (water), ξ means additional parallel vector k_z, a crucial momentum parameter, which controls the speed of the conversion process from the PWs to the SWs [22]. We provide the derivation for the general refractive-index distribution within Sec. I of the Supplemental Material [36]. With the length of the GIMs denoted by L, d is the thickness of the GIMs along the radial direction. In addition, g_1 and g_2, respectively, refer to the gradient factors of the upper-half

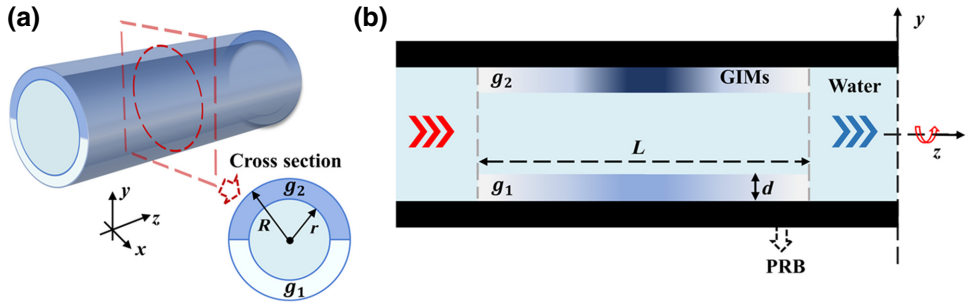

FIG. 1. Schematic plot of the acoustic waveguide mode converter. (a) For the 3D case, a circular waveguide with GIMs attached to its rigid wall, loaded with water (light blue region) as the inner core. Specifically, the GIM layer is divided into two symmetrical semiannulus regions in the x-y cross section, as shown in the inset map. (b) For the view of the x-z section, the proposed structure is constructed with a circular waveguide (denoted by the black region) and the two semicylindrical GIM layers (denoted by gradually blue regions). It is worth mentioning that the gradient-index profiles of the GIM layers are roughly characterized by gradient colors.

and lower-half GIMs. The key to achieving mode conversion is the difference between g_1 and g_2. According to Eq. (1), the range of refractive index is from 1 to $1 + g_2(\xi L/4k_0 d)$. Based on the coupled-mode theory, the mode-conversion effect is generated for the accumulated phase difference. It satisfies the phase-matching condition when the acoustic wave propagates between the upper-half and lower-half GIMs. In view of this configuration, the refractive-index distribution roughly changes with the shade of color. Throughout the study, we use software platform COMSOL Multiphysics to perform numerical simulations with the pressure acoustics model. The acoustic velocity of the GIMs is defined as $c = (\omega/k) = (\omega/nk_0)$, where ω is the angular velocity. However, those GIMs will inevitably induce shear wave, more discussion about the phase velocity for the transverse waves is discussed within Sec. II of the Supplemental Material [36].

Since the cut-off frequencies of mode (1,0) and mode (2,0) are 1831.5 and 3038.2 Hz, respectively, there are only two modes [the plane mode (0,0), mode (1,0)] exist in this range. More discussion on mode analysis can be found within Sec. III of the Supplemental Material [36]. To capture these modes while ensuring good nonreflecting effect at the waveguide inlet and outlet, two port boundary conditions are added at each end. Each port captures a specific mode, which means that on the inlet or outlet boundaries, the combination of ports defines the total acoustic field (sum of incident and outgoing waves) as

$$p_t = \sum_i (S_{i1} + A^{\text{in}}\delta_{i1})p_i, \tag{2}$$

where the summation i is over all ports on the given boundary (for example 3,4 on the outlet), A^{in} is the amplitude of the incident wave, and p_i is the mode shape of the ith port. The mode shape p_i is normalized to a unit maximum amplitude. The power of each mode can be further calculated by the sound pressure on the port. Here, P_{in} and P_{out} are the acoustic power at the inlet and outlet, respectively. The acoustic power is subject to the following relationship:

$$\begin{aligned} P_{\text{in}} &= \int_{\partial\Omega} \frac{{p_0}^2}{2\rho c} dA, \\ P_{\text{out}} &= \int_{\partial\Omega} \frac{|p_c|^2}{2\rho c} dA. \end{aligned} \tag{3}$$

Thus, the coefficients $P_{\text{out\_3}}$ and $P_{\text{out\_4}}$ describe the power of these eigenmodes at the output port. In general, the conversion efficiency can be expressed as

$$\eta = T \times f = \frac{P_{\text{out\_3}} + P_{\text{out\_4}}}{P_{\text{in\_1}}} \times \frac{P_{\text{out\_3}}}{P_{\text{out\_3}} + P_{\text{out\_4}}},$$

where T and f are the transmission of both modes and the fraction of the first mode.

In the simulations, the material parameters involved are set as follows: the length of the GIMs is $L = 200$ cm; $R = 24$ cm; $d = 2$ cm; $\xi = 0.2k_0$; $\rho = 1000$ kg/m^3, and $c = 1500$ m/s for water, where ρ and c are the density and velocity, respectively. For the plane acoustic wave incident from the left port, the 3D waveguide cloak can be achieved in the special case of $g_1 = g_2 = 1$, as shown in Fig. 2(a) (which has been discussed in Ref. [28]). In contrast, by slightly adjusting the lower-half GIM layer g_2 while keeping g_1 as constant, it is possible to achieve mode conversion from mode (0,0) to mode (1,0). As shown in Fig. 2(b), a perfect waveguide mode converter is realized at 2578 Hz for the case of $g_1 = 1$, $g_2 = 1.067$ with the fraction of desired mode f equal to 99.31% and the waveguide transmission T equal to 99.99%. Figure 2(c) refers to the cross section of the waveguide inlet and outlet, which reveals that the output mode turns into mode (1,0) completely. The numerical simulation definitely indicates that our scheme can be used as an excellent mode converter with negligible backscattering. It is noted that either adjusting g_1 or g_2 has the same effect. Figure 2(d) shows that the relationship between the fraction of the output mode (1,0) and the gradient factor of the lower-half GIM layer (g_2) as well as the working frequencies by fixing $g_1 = 1$. The white dashed line in Fig. 2(d) indicates the fraction of mode (1,0) in the outlet when $g_1 = 1$, $g_2 = 1.067$. There are several special areas in this frequency range (the corresponding transmission can be found within Sec. IV of the Supplemental Material [36]), indicating that there are some unideal dips caused by the Fano resonances [37]. When the related parameters of the circular waveguide are fixed, by carefully inspecting this frequency range, it is clearly seen that the output mode can be converted into mode (1,0) at multifrequencies. In addition, to avoid extreme accuracy of the refractive-index distribution, good results can also be achieved if the refractive distribution is not necessarily a linear function of the propagation distance. For detailed robust verification see Sec. V within the Supplemental Material [36].

Now, let us try to reveal the mechanism behind this scheme. The governing three-dimensional wave equation in a circular tube can be described in a cylindrical coordinate system:

$$\frac{1}{r}\frac{\partial}{\partial r}\left(r\frac{\partial p}{\partial r}\right) + \frac{1}{r^2}\frac{\partial^2 p}{\partial \theta^2} + \frac{\partial^2 p}{\partial z^2} = \frac{1}{c^2}\frac{\partial^2 p}{\partial t^2}, \tag{4}$$

where r, θ, z, and p are the radial distance, the polar angle, the tube axial distance and the acoustic pressure, respectively, c is the speed of sound in water and ω is the angular frequency. For the special case $g_1 = g_2 = 1$, assuming the inner media (water) is region I and the GIMs are region II, the general solution of Eq. (4) can be expressed as $p_1 = \text{A}J_m(k_{r1}r)\cos(m\theta + \varphi_m)e^{-jk_z z}$ (region I) and $p_2 = [BJ_m(k_{r2}r) + CN_m(k_{r2}r)]\cos(m\theta + \varphi_m)e^{-jk_x z}$

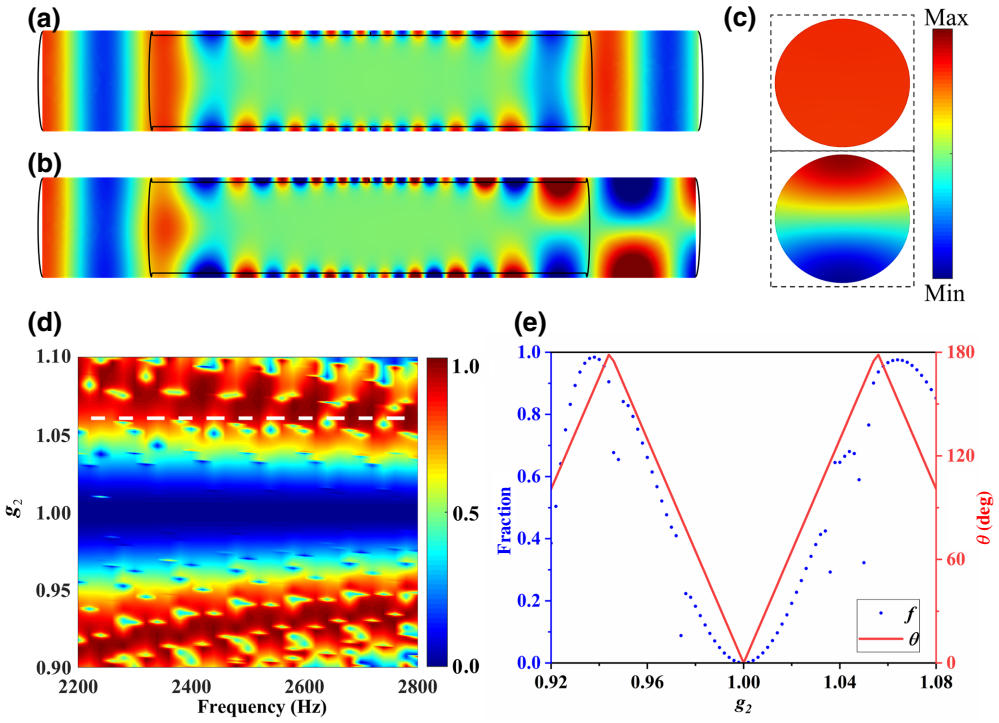

FIG. 2. Numerical simulations demonstrate that the zeroth acoustic mode can be converted to the first mode at multifrequencies. (a), (b) Simulated pressure field for acoustic wave incident from the left to right port at 2578 Hz with (a) $g_1 = g_2 = 1$ and (b) $g_1 = 1$, $g_2 = 1.067$. (c) The cross section of the ports on both ends in (b), respectively, realizing the conversion from the fundamental mode to the first mode. (d) The fraction of mode (1,0) f with different operating frequencies as well as the gradient factor of the lower-half GIM layer while the gradient factor of the upper-half GIMs is set as 1. The white dashed line in (d) refers to the frequency range from 2200 to 2800 Hz with $g_2 = 1.067$. (e) Illustration of accumulated phase difference (denoted by the red solid line) and the fraction of mode (1,0) on the outlet (denoted by the blue point) with varying gradient factors at 2700 Hz.

(region II). The wave vectors in the two regions have the following relationships: $k_{r1}^2 = k_0^2 - \beta^2$, $k_{r2}^2 = (nk_0)^2 - \beta^2$, where $k_0 = 2\pi f\,/c$, and β is the wave vector in the z direction for the two regions [28]. Therefore, the dispersion relation of the waveguide with GIMs at a fixed position can be obtained under the boundary conditions. As the refractive index of the GIMs increases, the dispersion curve of the zeroth mode corresponding to the waveguide cross section will gradually fall below the water line (acoustic cone in free space), which means that the wave vector of the propagating direction β is greater than k_0, and the k_{r1} will be an imaginary number. Therefore, the propagating wave will gradually be converted into the surface wave. When most energy is confined to the GIM region, the central energy becomes weaker and weaker, as if there is a forbidden zone in the middle of the waveguide that acoustic waves cannot pass through.

Due to a small gradient factor, propagating waves can be gradually converted to surface waves with negligible scattering. The divergence is the phase difference caused by the asymmetric gradient factors of the upper-half and lower-half GIM layers. The dispersion relation of circular waveguide is $\beta^2 + k_r^2 = k^2$, where β is the wave vector in the propagating direction (z axis). For convenience, β at a fixed position of GIM layer can be approximately equal to the wave vector in bulk material with the same parameters as the GIMs at this position. Furthermore, the phase difference accumulated between these two GIM layers can be established as $\theta = \int_{-L/2}^{L/2} \Delta\beta dx$. When θ is equal to $2n\pi\,(n = 0, 1, 2\ldots)$, there is no phase difference accumulated between the upper-half and lower-half GIM layers, so the output wave remains the same as the incident wave. While θ is equal to $2(n+1)\pi\,(n = 0, 1, 2\ldots)$, the phase-matching condition for achieving mode conversion can be satisfied: the output mode turns to mode (1,0). Figure 2(e) shows the fraction of output mode (1,0) and the phase difference θ as a function of g_2 with $g_1 = 1$ at the working frequency $f = 2700$ Hz, which coincides with our explanation very well. However, it is worth noting that this method is calculated based on the approximations mentioned above. Due to the coupling effect between the two GIMs and the Fano effect, the conversion efficiency will become undesired.

Based on the above-mentioned similar theory, it is entirely possible to consider higher-order mode conversion. In a higher frequency range (from 3038.2 to

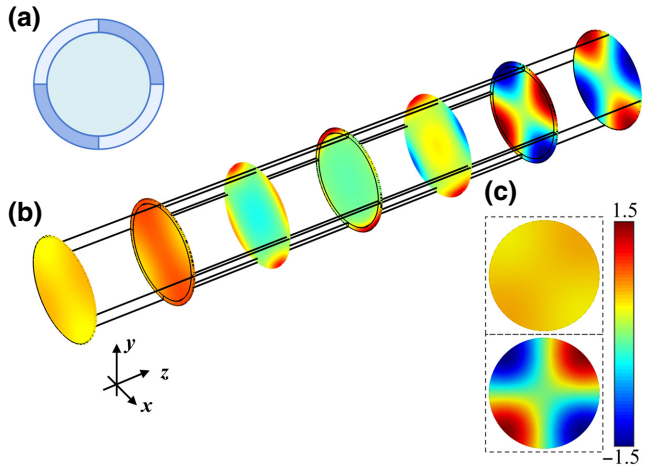

FIG. 3. (a) Cross section of the higher-order mode converter. The GIM layer attached to the wall is equally prorated into four regions, the darker blue region and the lighter blue region refer to g_1 and g_2, respectively. (b) The simulated phase distribution of the multiple x-y cross section in the waveguide with GIMs for the case where g_1 is equal to unity, g_2 is equal to 1.059 and the working frequency f is 3250 Hz. (c) Cross section of the ports on both ends in (b), respectively.

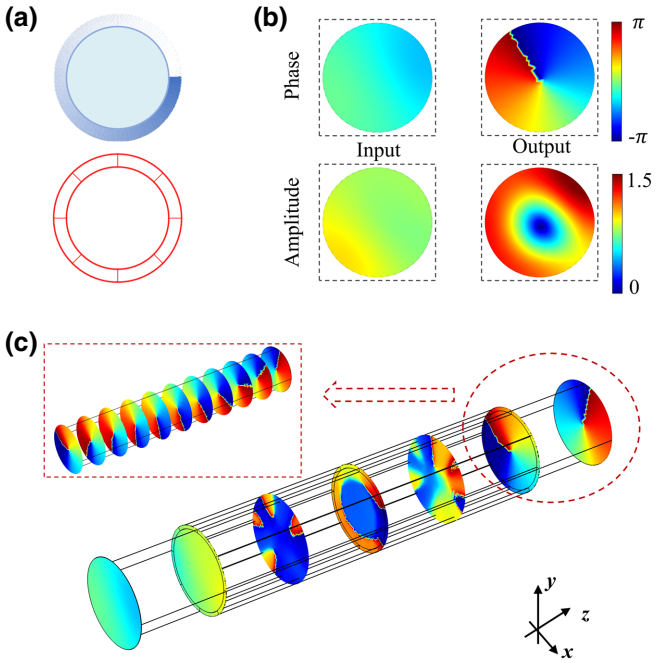

FIG. 4. (a) Cross section of the OAM generator with a topological charge $l = +1$. The gradient factor g of the GIM layer increases from 1 to 1.11 along the radial direction θ as the color changes. To simplify the implementation of the model, the GIM layer is divided into m subregions (here m is equal to 8) by partitioning the solid angles around the center points. Red lines denote the subregions profile. (b) Left panels: the calculated total pressure field in the inlet port (the phase distribution at the inlet and the corresponding amplitude distribution); right panels: the calculated output acoustic mode (the phase distribution at the outlet and the corresponding amplitude distribution). A helically phased vortex field with topological charge $l = +1$ can be produced. (c) Simulated phase distribution of the multiple x-y cross section in the waveguide with GIMs. For the incident plane acoustic wave from the left port, the output mode is converted into a vortex beam. The inset map of (c) shows an enlarged view of the dotted red region, which indicates that the obtained vortex beam can continue to propagate in the empty waveguide.

3811.5 Hz), three modes are supported in the output port of the waveguide, namely mode (0,0), mode (1,0), and mode (2,0). The difference with the above structure is that the GIM layer is divided into four regions as shown in Fig. 3(a), where dark blue regions represent the region with gradient factor g_1, light blue regions represent the region with gradient factor g_2. When the gradient factor g_2 is slightly modified by fixing $g_1 = 1$, mode conversion from mode (0,0) to mode (2,0) can be achieved. Figure 3(b) shows that, when g_1 and g_2 are set as 1 and 1.059, respectively, a nearly complete waveguide mode conversion is realized at 3250 Hz: the output mode turns into mode (2,0) with the fraction of desired mode f equal to 99.67% and the waveguide transmission T equal to 85.85%. Figure 3(c) refers to the cross section of the waveguide inlet and outlet, which further proves that the outlet mode is converted to mode (2,0) efficiently. However, the uneven intensity of the incident port is caused by backscattering. The reflection here is mainly due to the impedance mismatch between GIM layers with different gradient factors.

III. THE OAM GENERATOR VIA GRADIENT-INDEX METAMATERIALS

Furthermore, we also demonstrate a vortex-beam generator to extend the potentiality of our proposed mode-controlling method. In the previous example in Fig. 2, if θ equal to $(2n + 1)\pi (n = 0, 1, 2 \ldots)$, the acoustic pressure field through the upper-half GIMs has the opposite sign relative to the field through the lower-half GIMs. This also verified the conclusion that different parameters g accumulate different phase differences. It is therefore desirable that this scheme could be extended to generate a vortex wave. If the inner layer of the waveguide is divided into different areas and filled with appropriate linear gradient increment parameter g, a perfect OAM with a gradient phase distribution will be obtained in the outlet. For the case of the working frequency $f = 2700$ Hz, based on the above theory, a qualified phase difference can be achieved by adjusting the gradient factor g from 1 to 1.11, as shown in Fig. 4(a). In the virtual space, to avoid the extreme precision in the gradient factor depending on radial angle θ, we simplify it by partitioning the GIM layer into discrete subregions of eight different gradient factors. The gradient

factor g_m of each subregion can be given by

$$g_m = \frac{(g_{\max} - g_{\min})}{7}(m-1) + 1, m = 1, 2, \cdots 8, \quad (5)$$

where $g_{\min}$ and $g_{\max}$ are equal to 1 and 1.11, respectively. In the upper panels of Fig. 4(b), we show the simulated input-mode profiles and the corresponding phase distributions (the backscattering caused by the impedance mismatch leads to the uneven incident field). The lower panels show the simulated output-mode amplitude and the corresponding phase distributions: the output mode can be converted to a vortex beam with a topological charge $l = +1$ featured by its helical phase front and phase singularity [38,39]. In Fig. 4(c), we show the simulated phase distribution of the multiple x-y cross section in the waveguide with GIMs under the illumination of acoustic plane wave from the left port. The inset map of Fig. 4(c) illustrates an enlarged view of the dotted red region, which indicates that the obtained vortex beam can maintain the propagating mode in the empty waveguide at the right end. It is noted that there exists some backscattering due to the impedance mismatch between different subregions. Besides, the asymmetry of the structure will inevitably lead to slight uneven intensity distribution, which also does not affect the spiral distribution of the phase. Besides, the number of the GIM subregions can be further subdivided and increased to realize OAM waves with higher-order topology as shown in Fig. S8 (Sec. V) within the Supplemental Material [36].

IV. CONCLUSIONS

In this paper, we propose a multiple mode converter with highly efficient at multifrequency, by integrating the gradient-index metamaterials into a circular waveguide. With the rapid development of acoustic metamaterials, the range of refractive index required here is expected to be achieved with the help of soft porous silicone rubber materials. The efficient conversion to the desired mode is realized through constructive gradient-index metamaterials. Furthermore, we can realize a vortex beam with helical phase distribution by optimizing the gradient factors. We study analytically how conversion efficiency is affected by working frequencies and gradient factors, which verifies the simulation results. It is noted that when the distance between different subregions becomes smaller, the coupling effect will be stronger. As the Fano effect excites for higher-mode patterns, the mode conversion at some frequencies will be compromised. In addition to the above realized output modes, higher-order modes are expected to be implemented under this waveguide system (see Sec. III within the Supplemental Material [36]). Hence, the waveguide multimode converter may find potential applications in acoustic mode-diversion multiplexing for underwater acoustic communications.

ACKNOWLEDGMENT

This work is supported by the National Natural Science Foundation of China (Grants No. 11874311 and No. 92050102), the National Key Research and Development Program of China (Grant No. 2020YFA0710100), and the Fundamental Research Funds for the Central Universities (Grant No. 20720200074).

[1] M. Stojanovic, Recent advances in high-speed underwater acoustic communications, IEEE J. Oceanic Eng. **21**, 125 (1996).
[2] W. Scott Pegau, Deric Gray, and J. Ronald V. Zaneveld, Absorption and attenuation of visible and near-infrared light in water: Dependence on temperature and salinity, Appl. Opt. **36**, 6035 (1997).
[3] J. Carpenter, S. G. Leon-Saval, J. R. Salazar-Gil, J. Bland-Hawthorn, G. Baxter, L. Stewart, S. Frisken, M. A. F. Roelens, B. J. Eggleton, and J. Schröder, 1×11 few-mode fiber wavelength selective switch using photonic lanterns, Opt. Express. **22**, 2216 (2014).
[4] R. G. H. van Uden, R. Amezcua Correa, E. Antonio Lopez, F. M. Huijskens, C. Xia, G. Li, A. Schülzgen, H. de Waardt, A. M. J. Koonen, and C. M. Okonkwo, Ultra-high-density spatial division multiplexing with a few-mode multicore fibre, Nat. Photonics. **8**, 865 (2014).
[5] Y. Weng, T. Wang, and Z. Pan, Multi-functional fiber optic sensors based on mode division multiplexing[J], Opt. Mater. Express. **7**, 1917 (2017).
[6] Y. Jiao, S. Fan, and D. A. B. Miller, Demonstration of systematic photonic crystal device design and optimization by low-rank adjustments: An extremely compact mode separator, Opt. Lett. **30**, 141 (2005).
[7] B. Lee and S. Shin, Mode-order converter in a multimode waveguide, Opt. Lett. **28**, 1660 (2003).
[8] H. Guan, Y. Ma, R. Shi, A. Novack, J. Tao, Q. Fang, A. Lim, G. Lo, T. Baehr-Jones, and M. Hochberg, Ultracompact silicon-on-insulator polarization rotator for polarization-diversified circuits, Opt. Lett. **39**, 4703 (2014).
[9] X. Jiang, Y. Li, B. Liang, J. Cheng, and L. Zhang, Convert Acoustic Resonances to Orbital Angular Momentum, Phys. Rev. Lett. **117**, 034301 (2016).
[10] Z. Liu, X. Zhang, Y. Mao, Y. Y. Zhu, Z. Yang, C. T. Chan, and P. Sheng, Locally resonant sonic materials, Science. **2895485**, 1734 (2000).
[11] J. Li and C. T. Chan, Double-negative acoustic metamaterial, Phys. Rev. E. **70**, 055602 (2004).
[12] X. Zhu, B. Liang, W. Kan, X. Zou, and J. Cheng, Acoustic Cloaking by a Superlens With Single-Negative Materials, Phys. Rev. Lett. **106**, 014301 (2011).
[13] H. Jia, M. Ke, R. Hao, Y. Ye, F. Liu, and Z. Liu, Subwavelength imaging by a simple planar acoustic superlens, Appl. Phys. Lett. **97**, 173507 (2010).
[14] J. Zhu, J. Christensen, J. Jung, L. Martin-Moreno, X. Yin, L. Fok, X. Zhang, and F. J. Garcia-Vidal, A holey-structured metamaterial for acoustic deep-subwavelength imaging, Nat. Phys. **7**, 52 (2011).

[15] Y. Cheng, C. Zhou, Q. Wei, D. Wu, and X. Liu, Acoustic subwavelength imaging of subsurface objects with acoustic resonant metalens, Appl. Phys. Lett. **103**, 224104 (2013).
[16] H. Chen and C. T. Chan, Acoustic cloaking in three dimensions using acoustic metamaterials, Appl. Phys. Lett. **91**, 183518 (2007).
[17] S. A. Cummer and D. Schurig, One path to acoustic cloaking, New J. Phys. **9**, 45 (2007).
[18] A. Ba, A. Kovalenko, C. Aristégui, O. Mondain-Monval, and T. Brunet, Soft porous silicone rubbers with ultralow sound speeds in acoustic metamaterials, Sci. Rep. **7**, 1 (2017).
[19] G. T. Kuster and M. N. Toksöz, Velocity and attenuation of seismic waves in two-phase media: Part I. Theoretical formulations, Geophysics. **39**, 587 (1974).
[20] K. Zimny, A. Merlin, A. Ba, C. Aristégui, T. Brunet, and O. Mondain-Monval, Soft porous silicone rubbers as key elements for the realization of acoustic metamaterials, Langmuir. **31**, 3215 (2015).
[21] Y. Jin, R. Kumar, O. Poncelet, O. Mondain-Monval, and T. Brunet, Flat acoustics with soft gradient-index metasurfaces, Nat. Commun. **10**, 1 (2019).
[22] S. Sun, Q. He, S. Xiao, Q. Xu, and L. Zhou, Gradient-index meta-surfaces as a bridge linking propagating waves and surface waves, Nat. Mater. **11**, 426 (2012).
[23] Y. Xu, C. Gu, B. Hou, Y. Lai, J. Li, and H. Chen, Broadband asymmetric waveguiding of light without polarization limitations, Nat. Commun. **4**, 1 (2013).
[24] H. Wang, Y. Xu, P. Genevet, J. Jiang, and H. Chen, Broadband mode conversion via gradient index metamaterials, Sci. Rep. **6**, 24529 (2016).
[25] C. Gu, Y. Xu, S. Li, W. Lu, J. Li, H. Chen, and B. Hou, A broadband polarization-insensitive cloak based on mode conversion, Sci. Rep. **5**, 12106 (2015).
[26] S. Zhu, Y. Cao, Y. Fu, L. Gao, X. Li, H. Chen, and Y. Xu, 3D broadband waveguide cloak and light squeezing in terahertz regime, Opt. Lett. **45**, 652 (2020).
[27] W. Cao, L. Wu, C. Zhang, J. Ke, Q. Cheng, T. Cui, and Y. Jing, Asymmetric transmission of acoustic waves in a waveguide via gradient index metamaterials, Sci. Bull. **64**, 808 (2019).
[28] C. Hu, Y. Zeng, Y. Liu, and H. Chen, Three-dimensional broadband acoustic waveguide cloak, chin. Phys. Lett. **37**, 054302 (2020).
[29] S. Zou, Y. Xu, R. Zatianina, C. Li, X. Liang, L. Zhu, Y. Zhang, G. Liu, Q. H. Liu, H. Chen, and Z. Wang, Broadband Waveguide Cloak for Water Waves, Phys. Rev. Lett. **123**, 074501 (2019).
[30] S. Ouyang, H. He, Z. He, K. Deng, and H. Zhao, Acoustic one-way mode conversion and transmission by sonic crystal waveguides, J. Appl. Phys. **120**, 104504 (2016).
[31] A. Yariv and P. Yeh, *Optical Wave in Crystals: Propagation and Control of Laser Radiation* (Wiley Interscience, New York, 2002).
[32] A. W. Snyder and J. Love, *Optical Waveguide Theory* (Springer Science &Business Media, Berlin, 2012).
[33] A. Marzo A, S. A. Seah, B. W. Drinkwater, D. R. Sahoo, B. Long, and S. Subramanian, Holographic acoustic elements for manipulation of levitated objects, Nat. Commun. **6**, 8661 (2015).
[34] D. Baresch, J. L. Thomas, and R. Marchiano, Observation of a Single-Beam Gradient Force Acoustical Trap for Elastic Particles: Acoustical Tweezers, Phys. Rev. Lett. **116**, 024301 (2016).
[35] X. D. Fan and L. K. Zhang, Trapping Force of Acoustical Bessel Beams on a Sphere and Stable Tractor Beams, Phys. Rev. Appl. **11**, 014055 (2019).
[36] See Supplemental Material at http://link.aps.org/supplemental/10.1103/PhysRevApplied.15.014035 for the following five sections: Sec. I. The detailed definition about the index profile. Sec. II. The influence of shear waves based on the acoustic-solid interaction model. Sec. III. Mode analysis and the effect of higher-order mode converter. Sec. IV. Special cases caused by Fano resonances. Sec. V. The feasibility of the discretized structure.
[37] Y. Xu, S. Li, B. Hou, and H. Chen, Fano resonances from gradient-index metamaterials, Sci. Rep. **6**, 19927 (2016).
[38] Y. Shen, X. Wang, Z. Xie, C. Min, X. Fu, Q. Liu, M. Gong, and X. Yuan, Optical vortices 30 years on: OAM manipulation from topological charge to multiple singularities, Light: Sci. Appl. **8**, 1 (2019).
[39] W. Y. Tsai, Q. Sun, G. Hu, P. C. Wu, R. J. Lin, C. W. Qiu, K. Ueno, H. Misawa, and D. P. Tsai, Twisted surface plasmons with spincontrolled gold surfaces, Adv. Opt. Mater. **7**, 1801060 (2019).